Journal of Applied Physics ARTICLE pubs.aip.org/aip/jap

Triple evaporation growth and photoemission characterization of bialkali antimonide photocathodes

Cite as: J. Appl. Phys. **138**, 045704 (2025); doi: 10.1063/5.0268697
Submitted: 3 March 2025 · Accepted: 3 July 2025 ·
Published Online: 25 July 2025

J. Dube,[1,2,a)] J. Kühn,[1,b)] C. Wang,[1,3] S. Mistry,[1] G. Klemz,[1] A. Galdi,[1,4] and T. Kamps[1,2]

AFFILIATIONS

[1]Helmholtz-Zentrum Berlin für Materialien und Energie GmbH, Hahn-Meitner-Platz 1, 14109 Berlin, Germany
[2]Institut für Physik, Humboldt-Universität zu Berlin, Newton-Straße 15, 12489 Berlin, Germany
[3]Institut für Werkstofftechnik, Universität Siegen, Paul-Bonatz-Straße 9-11, 57076 Siegen, Germany
[4]Dipartimento di Ingegneria Industriale, Università degli Studi di Salerno, 84084 Fisciano (SA), Italy

[a)]**Author to whom correspondence should be addressed:** jonas.dube@helmholtz-berlin.de
[b)]**Electronic mail:** julius.kuehn@helmholtz-berlin.de

ABSTRACT

The development of high-performance photocathodes is essential for generating high-brightness electron beams required by existing and future accelerators. This work introduces a state-of-the-art triple evaporation growth system designed for bialkali antimonide photocathodes. By enabling the simultaneous deposition of all three materials, this system significantly enhances vacuum stability and the reproducibility of photocathode fabrication. Complementing this, a novel characterization system allows spatially and spectrally resolved measurements of key photocathode parameters, such as quantum efficiency (QE), mean transverse energy (MTE), reflectance, and lifetime. Crucially, all measurements are performed within a single compact setup, without moving the sample, preserving ultrahigh vacuum conditions. The spectral resolved measurement of the reflectance allows the investigation of the color. Photocathode colorimetry may provide valuable insights into material homogeneity and aging. A Na–K–Sb photocathode was grown using the triple evaporation method, achieving an initial QE of 5.5% at 520 nm. The photocathode was characterized over 2 months, and MTE measurements were performed with two different methods. A dataset with spectral response, reflectance, and colorimetry data was recorded. Together, the triple evaporation growth and the characterization system mark a significant advancement in optimizing photocathodes with exceptional performance, paving the way for brighter and more stable electron sources for next-generation accelerator facilities.

I. INTRODUCTION

The generation of high-brightness electron beams plays a significant role for advanced accelerator facilities such as energy recovery linacs (ERLs),[1,2] free-electron lasers (FELs),[3,4] and ultrafast electron diffraction (UED) systems.[5–7] Since the performance of all these systems is predominantly determined by the electron source, photocathodes are used to meet the high requirements. The electron yield and the intrinsic emittance of the photocathode define the brightness limits for the accelerator.[8] These properties are described by the quantum efficiency (QE) and the mean transverse energy (MTE). Together with the lifetime, they are the physical key parameters to describe the performance of a photocathode. While the QE defines the electron yield, the MTE is closely related to the normalized emittance $\epsilon_{x,y}$ of the emitted electron beam as shown in Eq. (1). Here, $\sigma_{x,y}$ describes the spot size of the illuminating light at the photocathode surface, and m_e and c are the electron mass and the vacuum speed of light, respectively,[9]

$$\epsilon_{x,y} = \sigma_{x,y}\sqrt{\frac{\mathrm{MTE}}{m_e c^2}}. \tag{1}$$

Improvements here will have substantial impact on the performance of the accelerator, for example, a lower emittance leads to a

shorter gain length at FEL applications.[10] Another important parameter is the reflectance of the photocathode surface, as it influences the QE of the photocathode.[11] The reflectance should be low because a reflected photon cannot contribute to the photoemission process.

Bialkali antimonide photocathodes, such as Cs–K–Sb, Rb–K–Sb, or Na–K–Sb, offer a high QE and low MTE and can photoemit when illuminated with visible light.[12] Hence, they are suitable candidates to produce high-brightness electron beams.

Sometimes, the photocathode growth system is attached to the photoinjector, more often it is in a separate laboratory for more flexibility. In this case, a vacuum transport system is required due to its high sensitivity to residual gases.[13,14] Therefore, the photocathodes must remain under ultrahigh vacuum conditions with at least low 10^{-9} mbar during growth, characterization, and operation in a photoinjector, including the transfer between the different systems.[15]

At Helmholtz-Zentrum Berlin (HZB), bialkali antimonide photocathodes are developed and investigated for several years for high average current and low emittance ERL applications.[15–17] The photocathodes were prepared using the traditional method of sequential deposition of each element or co-deposition of the alkali metals and optimized with respect to their QE and lifetime.[18,19] In 2024, a newly designed preparation chamber for the growth of bialkali antimonide photocathodes by triple evaporation of the three elements was commissioned.

Simultaneously, the Photoemission and Transverse Energy Experiment (PhoTEx) has been set up to measure all physical key parameters of the photocathodes, including the MTE. The system is based on the method of acceleration and subsequent free expansion of the electron beam.[9] The MTE can be determined from the size of the electron beam at the detector. There are existing instruments based on this principle such as the TEmeter from Lee *et al.*[9] and the momentatron presented by Feng *et al.*[20] A modified version is the TESS system developed by Jones *et al.*,[21] and a new system is under construction by Sertore *et al.*[22] Based on these systems, we developed a novel instrument that is presented here. Additionally, this instrument is able to measure the QE and reflectance in one compact setup and can be used for lifetime studies.

The paper is structured in four parts: After an overview about the boundary conditions for the photocathode laboratory, the new triple evaporation growth system is described, followed by a description of the MTE measurement device—PhoTEx. In the last part, the growth of the first triple evaporation Na–K–Sb photocathode and its characterization at the PhoTEx instrument is presented.

II. PHOTOCATHODES FOR AN SRF GUN

The photocathodes grown at HZB are developed and investigated for use in the SRF photoinjector of the Superconducting RF Electron Accelerator Laboratory (SEALab, formerly bERLinPro).[2,23,24] Using an SRF photoinjector places high demands on the thermal and electric properties of the photocathode and the plug. A cylindrical plug with 10 mm diameter is used as a substrate for the growth of the photocathodes. The design is specially adapted for the SRF photoinjector of SEALab and was extensively tested for operation.[25] It is made of molybdenum to meet the high thermal and electrical requirements and is optimized to avoid field emission in strong acceleration fields.[18,26] During operation, electric fields up to 20 MV/m may be applied to the cathode with an operating temperature between 80 K and room temperature.

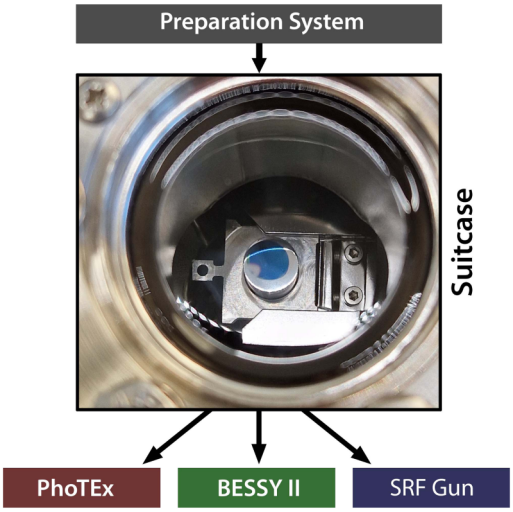

FIG. 1. Omicron sample holder with photocathode TWH13 in the suitcase; a suitcase is used to transfer samples from the photocathode preparation chamber to the SEALab SRF gun or characterization systems like PhoTEx and beamlines at the synchrotron radiation source BESSY II.

The photocathodes are developed and tested on the same substrate that will later be used in the photoinjector. The plugs are mounted on an adapted Omicron flag style sample holder for preparation, characterization, and transfer as shown in Fig. 1. At the photoinjector, the plug is removed from the sample holder and inserted into the injector.[26] During the transfer, the photocathodes must remain particulate free and under ultrahigh vacuum conditions of at least low 10^{-9} mbar due to their high chemical reactivity. A vacuum suitcase was built to transfer the samples between different facilities such as the preparation system, the SRF gun or characterization systems like PhoTEx, or beamlines at the BESSY II synchrotron radiation facility at HZB.

The use of the photocathode in an SRF gun sets the boundary conditions for the transfer, characterization, and the preparation of the photocathodes.

III. TRIPLE EVAPORATION GROWTH SYSTEM

A new photocathode preparation chamber was commissioned in summer 2024 to provide more flexibility in photocathode growth. In our previous setup, Sb and the alkali metals could not be deposited together. First, an Sb layer was deposited, and the alkali metals were evaporated sequentially or co-deposited afterward.[15,18] This limited the ability to develop new growth recipes. Sb was evaporated from an effusion cell, while SAES dispensers were used for the alkali metals. Therefore, parts of the vacuum chamber had to be regularly vented to change the dispensers.

In the new setup, the alkali dispensers were replaced by effusion cells filled with SAES AlkaMax pills. The antimony is evaporated from beads in a thermal cracker cell. The three sources are oriented so that they all point toward the substrate position to allow simultaneous evaporation of the three materials. The thermal cracker cell for antimony is placed above the photocathode at an angle of 52° at a fixed distance of 148 mm. The alkali effusion cells are located in the horizontal plane at an angle of 30° to the normal of the photocathode surface. The distance of the alkali metal sources can be adjusted with a Z-drive and is typically set to 60 mm. The photocathode is placed on a heatable XYZΦ manipulator. A circular 8 mm aperture is placed in front of the plug to achieve a well-defined photocathode area on the substrate. The aperture has a bevelled edge to reduce shadowing effects from the sources and increase the area of full overlap of all three materials. The deposition rate can be measured using a water-cooled quartz crystal microbalance (QCM) placed in the same position as the plug during the calibration measurement. The rate can be adjusted by the temperature settings of the sources. Additionally, an argon sputter gun is attached to the system for the cleaning of the plug surface.

The photocathode can be illuminated directly from the front with the spectral response setup. A xenon lamp and a monochromator are used to generate monochromatic light with a bandwidth of 5 nm in the full visible regime. A pick-up anode is placed close to the photocathode and is connected to a picoammeter to measure the extracted current. The calculation of the QE is described in more detail in Sec. IV C 1. During the growth of a photocathode, the light source is changed to a 520 nm laser with a maximum output of 0.9 mW, to increase the sensitivity especially at the beginning of the growth. The light power can be adjusted with neutral density filters.

The vacuum is maintained by a turbo pump, an ion getter pump (IGP), and a nonevaporable getter (NEG) pump. The partial pressure of any residual gases can be measured with a residual gas analyzer (RGA). After bakeout, a base pressure of 9×10^{-11} mbar was achieved. The preparation system is attached to an analysis chamber for x-ray photoelectron spectroscopy (XPS) measurements[15] and to a load lock to insert new samples. A second load lock is located at the back of the vacuum system to transfer the photocathodes to other facilities such as PhoTEx or the photoinjector of SEALab.

A. Suitcase for sample transfer

A new suitcase was built, to transfer the samples at ultra high vacuum conditions. The suitcase is equipped with a pincer connected to a transfer arm. Therefore, no transfer mechanism is required at the receiving laboratory. Hence, it is compatible with most vacuum systems. A parking stage allows the simultaneous transfer of up to three samples. A nonevaporable getter (NEG) pump is used to achieve a base pressure of 3×10^{-11} mbar. Only during the gripping of a sample the pressure may temporarily increase due to degassing of the transfer arm. An additional IGP can be used to increase the pumping speed. During a transfer to another laboratory, the IGP and the vacuum gauge are connected to an uninterruptible power supply. The whole suitcase is mounted on wheels and is height adjustable. Therefore, it can be flexibly adjusted to different systems.

IV. CHARACTERIZATION SYSTEM PhoTEx

The **Pho**toemission and **T**ransverse **E**nergy E**x**periment—PhoTEx—is an instrument to characterize the physical key parameters of photocathodes for electron accelerators. Besides the MTE, also the QE, reflectance and lifetime can be investigated at PhoTEx. Spectrally resolved measurements of all parameters are possible across the full visible regime. This is of major importance as the photoemission process is primarily determined by the energy of the incident photons $\hbar\omega$ and the effective workfunction of the material ϕ_{eff}.[11,27,28] The difference of both values is defined as the excess energy $E_{\text{excess}} = \hbar\omega - \phi_{\text{eff}}$. As a first approximation, the MTE and QE can be described by the excess energy as shown in Eq. (2).[11] The equation for the QE is valid close to the threshold energy, while the MTE formula is an approximation for high excess energies,

$$\text{QE} \propto E_{\text{excess}}^2 \quad \text{MTE} = \frac{E_{\text{excess}}}{3}. \tag{2}$$

Deviations to this first approach may occur for semiconducting materials and at nonzero temperature.[11] Close to the threshold energy, the MTE is no longer linear but saturates at the thermal limit $k_B T$, where k_B is the Bolzmann constant.

A. Experimental setup

For the MTE measurement, a negative voltage U is applied to the photocathode, and a conductive copper grid is placed at distance g to achieve a homogeneous electric field as shown in Fig. 2. The grid has square holes with a size of 11 μm and an open area of 55%. After the electrons pass through the grid, they enter a field free region. The electron beam is expanding in this drift tube of length d to increase the spatial resolution at the detector. With the assumption of a perfect homogeneous field and field free drift region, Eq. (3) can be derived to determine the MTE from the rms

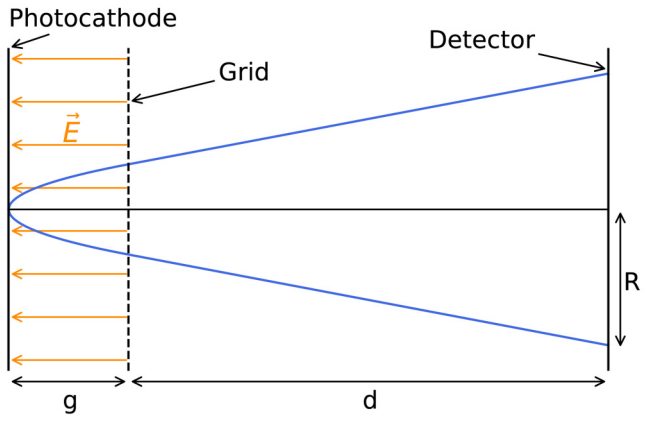

FIG. 2. Schematic of the measurement principle of PhoTEx. The electrons are accelerated in a homogeneous E-field (orange) between the negatively biased photocathode and a grounded grid. After passing the grid, the electron beam expands freely until it hits the detector. The mean transverse energy can be determined from the rms offset at detector *R*.

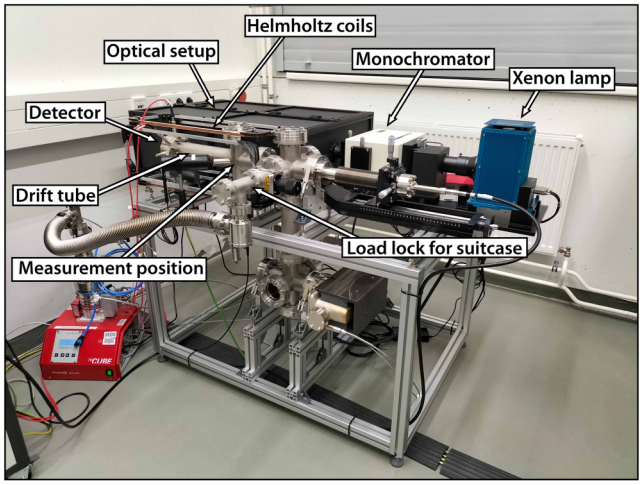

FIG. 3. PhoTEx assembled in the MTE laboratory at HZB.

radius R of the electron beam at the detector,[22]

$$\mathrm{MTE} = \frac{R^2}{(2g+d)^2}\,Ue. \tag{3}$$

The detector is a one-stage microchannel plate (MCP) with a gain up to 10^4 and a P43 phosphor screen. A characterization of the detector in our laboratory showed a doubling of the intensity every 36 V.

The whole PhoTEx setup is shown in Fig. 3 and contains three different parts: the vacuum chamber, an optical setup, and Helmholtz coils to steer the electron beam on the detector. A photocathode can be transferred to PhoTEx with the vacuum suitcase mentioned above. The suitcase is attached to the load lock of PhoTEx, which can be separately pumped with a pumping cart. The photocathode is moved with an XYZ manipulator to the measurement position at 10 mm distance in front of the grid. The XY stage of the manipulator allows spatially resolved characterization of the photocathode. A nonevaporable getter pump and an ion getter pump ensure a vacuum base pressure of 5×10^{-11} mbar. A copper rod is mounted on a Z-drive below the measurement position. When inserted, it is placed between the photocathode and the grid and acts as a pick-up anode to measure the quantum efficiency.

The grid of 8 mm diameter is surrounded by a molybdenum (Mo) shield of 64 mm diameter. This enables a better shielding for the drift tube and a more homogeneous electric field in the acceleration gap. The incident and reflected light passes through holes in the Mo shield of 3.5 mm diameter as shown in Fig. 4. With that, we achieve an illumination angle of 38.7°. However, the optical path is very sensitive to misalignments.

The light source used at PhoTEx is a 75 W Xenon lamp connected to a monochromator. This allows the illumination of the photocathode with monochromatic light in the regime of (400–700) nm with a bandwidth of 5 nm. Three lenses are used to image an iris aperture onto the photocathode surface with a demagnification of 10:1. A beam splitter is placed just before the light enters the vacuum chamber to allow live monitoring of the optical power as shown in Fig. 5. An identical vacuum window is placed in this reference light path to achieve the same conditions as at the photocathode. The spot size of the light beam can be measured using a beam profiler that is located at the reference light path. The lens system is adjusted so that the photocathode and the beam profiler are located at the focal point with a deviation of ± 2 mm. The 1σ radius of the Gaussian light spot was measured in this area and is $\sigma = (43 \pm 3)\,\mu$m. Since the photocathode is placed at the

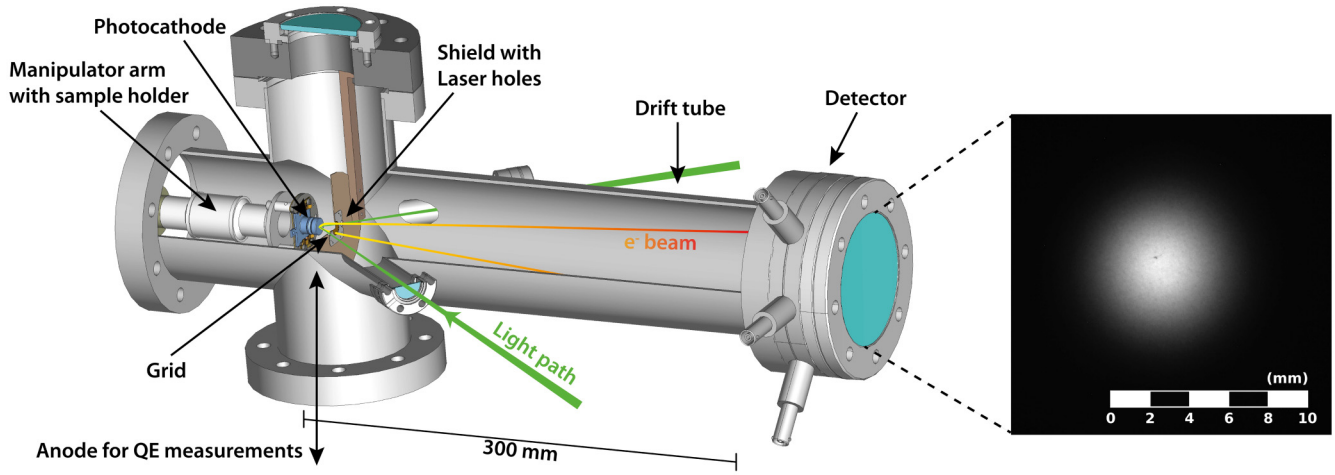

FIG. 4. Illustration of the analysis chamber of PhoTEx. The 3D model is sectioned for a better visualization. A real image of an electron beam at the detector is shown on the right. An anode can be moved in from the bottom with a Z-drive for QE measurements.

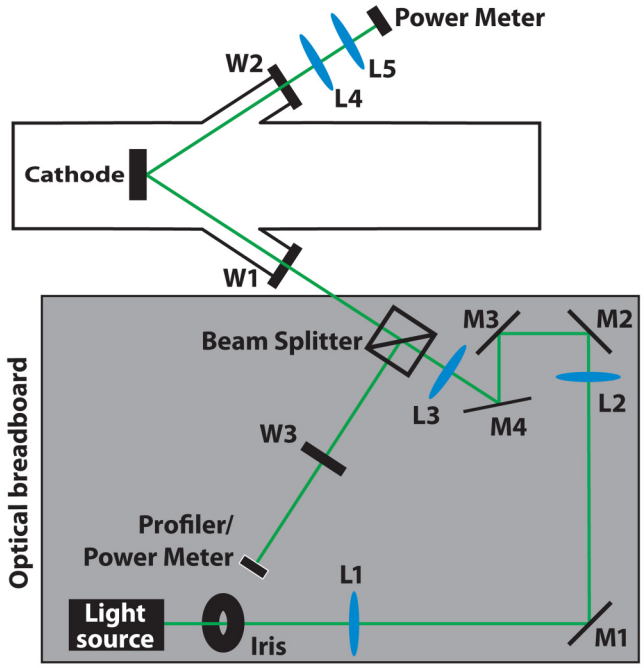

FIG. 5. Schematic of the optical setup at PhoTEx. Three lenses (L) are used to image an iris onto the photocathode. Mirrors (M) are used to fold the optical path. The light enters and exits the vacuum chamber through vacuum windows (W). An identical window is placed in the reference light path (W3).

focal point, the reflected beam is strongly divergent. Two additional lenses are used to focus the reflected beam onto the second power meter to measure the reflectance. The optical density of these lenses was measured and is considered in the calculation of reflectance. Neutral density (ND) filters can be placed in the optical path to reduce the optical power. A reduced optical power leads to a lower photocurrent and, therefore, reduces space charge effects.

The electrons are very sensitive to external fields due to their low kinetic energy. The magnetic field strength of the Earth would already be enough that the electrons are not hitting the detector anymore. Helmholtz coils are used to compensate external magnetic fields at PhoTEx. Only the magnetic field components perpendicular to the velocity are deflecting the electrons. Simulations confirmed that the longitudinal component of the magnetic field is negligible. Therefore, only the transverse field components have to be compensated. Two pairs of rectangular Helmholtz coils are placed around the analysis chamber at PhoTEx. The coils create a homogeneous magnetic field in the acceleration gap and the drift tube and allow steering of the electron beam to the center of the detector. The technical data of the full PhoTEx setup is summarized in Table I.

B. Particle tracking simulation

The assumption of a perfect homogeneous electric field between the cathode and the grid and a perfect field free drift region cannot be achieved in reality. The measurement of the MTE was simulated to quantify the impact of field imperfections and determine an instrument function to correct for these deviations.

The electric field in the measurement region was simulated with CST Studio Suite[29] on a three-dimensional grid. In Fig. 6 a constant voltage of 5000 V was applied to the surface of the photocathode. The grid, vacuum chamber, and detector have a potential of 0 V. In the case of a perfect homogeneous field, we would expect a constant field strength of 0.5 MV/m between the photocathode and the grid. As shown in Fig. 6, the field is decreasing from 0.69 MV/m at the photocathode surface to 0.38 MV/m at the grid

TABLE I. Technical data of PhoTEx. Listed are the parameters for the vacuum system, optics, and magnetic shielding.

Sample holder:	Omicron flag style
Base pressure:	5×10^{-11} mbar
Acceleration gap:	10 mm
Drift distance:	300.9 mm
Acceleration voltage:	<6.5 kV
Max. E-field:	0.65 MV/m
Grid:	11 μm hole size, 55 % open area
Detector:	One stage MCP + P43 phosphor screen
Light source:	Zolix tunable light source TLS2-X75A-G; 75W Xenon lamp + Monochromator
Spectral regime:	(400–700) nm
Bandwidth:	5 nm
Spot size at cathode:	1σ diameter = $(86 \pm 6)\,\mu$m
Illumination angle:	38.7°
Magnetic shielding:	Helmholtz coils for transverse directions

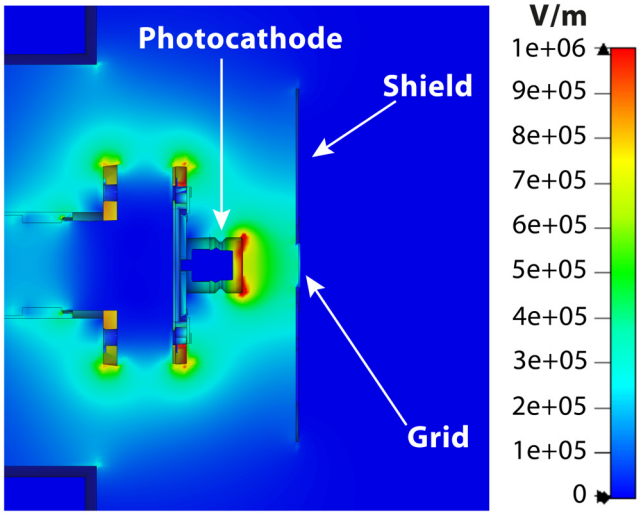

FIG. 6. Simulation of the electric fields in the analysis chamber of PhoTEx. The field between the photocathode and the grid is not perfectly homogeneous. A good electrical shielding to the drift tube is achieved by the grid and the shield.

in reality. This will also influence the trajectories of the emitted electrons and hence the spot size of the electron beam at the detector.

Electron distributions with a specified MTE were tracked through the simulated E-fields with the particle tracking algorithm ASTRA[30] to simulate the electron distribution at the detector. The simulation was performed for a range of different start values, i.e., different voltages from 500 V to 6.5 kV, different MTE's and light spot sizes at the photocathode surface. Each time, a distribution of 100 000 electrons was tracked through the simulated electric fields inside PhoTEx. A radial intensity function of the generated detector image was calculated to determine the beam radius, as described in Sec. IV C. This simulated measurement R_{meas} was then compared with the theoretically expected value R from Eq. (3). The relation between the measured value and the expected value is generally linear, with a gradient of $\alpha \approx 0.87$, meaning that R is about 13 % smaller than the measured value. This is due to the imperfection in the electric fields shown in Fig. 6, which lead to a defocusing of the electron beam.

The theory in Eq. (3) assumes a point-like emission area of the electrons, but in reality, the electron distribution at the detector is a superposition of the transverse energy and the initial spatial distribution of the electron, i.e., the light spot size at the photocathode surface. Hence, the measured radius is saturating for small radii. This effect is negligible if the spot size of the electron beam at the detector is much larger then the light spot at the photocathode surface. Therefore, the light spot at the cathode should be small. At PhoTEx, the 1σ radius of the spot at the photocathode surface is $\sigma = (43 \pm 3)\,\mu\mathrm{m}$. The simulations showed that this spot size is sufficiently small that the relation between the measured radius and the expected value can be assumed to be linear. The instrument function in Eq. (4) was developed to correct the measured radius for this specific spot size of the illuminating light. The parameters α and β were found by fitting this function to the simulated data, where α describes the difference between the expected and measured radius and β corrects for the extended emission area,

$$\begin{gathered} R = \alpha \times R_{\mathrm{meas}} - \beta, \\ \alpha = 0.873 \qquad \beta = 1.61 \times 10^{-4}\,\mathrm{m}. \end{gathered} \tag{4}$$

The deviation between the measured and the real value can be significantly reduced by correcting the measurement with the instrument function. The remaining uncertainty U_R is dependent on the measured radius and is listed below:

$$\begin{aligned} R_{\mathrm{meas}} < 2.5\,\mathrm{mm} &\rightarrow U_R = 4\%, \\ 2.5\,\mathrm{mm} < R_{\mathrm{meas}} < 11\,\mathrm{mm} &\rightarrow U_R = 2\%, \\ 11\,\mathrm{mm} < R_{\mathrm{meas}} &\rightarrow U_R = 4\%. \end{aligned}$$

C. Data acquisition and analysis

1. Spectral response

During a spectral response measurement, the iris aperture can be opened to increase the optical power and, therefore, improve the signal-to-noise ratio. A wavelength scan is performed with a step width of 5 nm, and the optical power P_γ and the photocurrent I_e are measured simultaneously. The photocurrent is averaged over 20 data points to reduce noise. The standard deviation of the measurements is the largest contribution to the total uncertainty of the measured QE, especially for low currents. The optical background power and the darkcurrent are measured and subtracted from the measurement. The QE is then calculated for each wavelength λ with Eq. (5).[8] Here, N_e is the number of electrons extracted, N_γ is the number of incident photons, and h and c are the Planck constant and the vacuum speed of light, respectively,

$$\mathrm{QE} = \frac{N_e}{N_\gamma} = \frac{I_e hc}{P_\gamma \lambda e}. \tag{5}$$

2. Reflectance and colorimetry

For a reflectance measurement, the wavelength is scanned with the monochromator, and the initial and reflected optical power is measured with two power meters. The reflectance is calculated from the ratio of both measurements. Here, also the transmission of the viewport and lenses used to focus the reflected beam onto the second power meter are taken into account.

From the measured reflectance curve, the color of the photocathode can be derived using the CIE 1931 color space. It is merely a distinct mode of presentation and does not possess more information. However, it is a good way to make the reflectance data more tangible, as it corresponds to our human perception. With this method, the color of the photocathodes can be studied in a systematic way. It may provide valuable insights into the homogeneity of the photocathode film and could facilitate a preliminary assessment of the photocathode quality in the future.

The tristimulus values X, Y, and Z are calculated from the measured spectral reflectance R_λ using the CIE color-matching functions $\bar{x}$, $\bar{y}$, and $\bar{z}$ and the spectral power distribution S of a specified illuminant using Eq. (6).[31] The sum is performed from 400 to 700 nm in steps of 5 nm. The standard illuminant D65 and the CIE 1931 color-matching functions for a 2° observer are used for our data analysis.[32,33] k is a normalization constant such that 1 is the maximum value for Y,

$$\begin{aligned} X &= k \sum_\lambda S_\lambda R_\lambda \bar{x}_\lambda, \\ Y &= k \sum_\lambda S_\lambda R_\lambda \bar{y}_\lambda, \\ Z &= k \sum_\lambda S_\lambda R_\lambda \bar{z}_\lambda, \\ k &= \sum_\lambda \frac{1}{S_\lambda \bar{y}_\lambda}. \end{aligned} \tag{6}$$

The tristimulus values can be converted to the sRGB color space for display on computer screens.

3. Mean transverse energy

The MTE can be determined with Eq. (3), with R being the root-mean-square radius of the electron beam. For the measurement, a data image is taken with the detector camera and corrected

by subtraction of a dark image. The dark image is taken without illuminating the photocathode but with the same exposure time and applied voltages. A mask is applied to remove all pixels outside the detector area. A 3D Gaussian fit is applied to the resulting image with an independent variance in both directions. The radius of the electron distribution is then given by $R = \sqrt{\sigma_x^2 + \sigma_y^2}$. This formula reduces to $R = \sqrt{2}\sigma$ with $\sigma = \sigma_x = \sigma_y$ as we expect a radial symmetry. From the 3D Gaussian, the center of the distribution is known. A radial intensity function (RIF) is calculated by averaging the intensity of all pixels with equal distance to the center to reduce noise. A Gaussian fit is applied to the RIF and the radius is determined as described in Eq. (7). The conversion factor f_c is used to convert the number of pixels into a distance,

$$R = \sqrt{2}\sigma \times f_c. \tag{7}$$

A detector image and the associated RIF are shown in Fig. 7. The resulting radius is corrected by the instrument function Eq. (4) derived in Sec. IV B. The total uncertainty of the radius is given by the uncertainty of the instrument function discussed above, the resolution of the detector, the fit uncertainty of the RIF, and the Davisson–Calbick lens effect. The latter describes the deflection of an electron at the edge of a hole at the copper grid due to the bending of electric fields. This angle deviation can be described with Eq. (8).[34,35] Here, D is the width of a grid cell and g is the distance between the photocathode and the grid,

$$\Theta = \frac{D}{8g}. \tag{8}$$

The deviation at the detector is then given by $\Delta R_2 = \tan(\Theta)d$, with d being the distance between the grid and the detector. The Davisson–Calbick effect is not randomly distributed but primarily leads to an increase in the measured radius. Therefore, this effect is linearly added to the total uncertainty of the radius $\Delta R_{\text{tot}} = \sqrt{\Delta R_1^2 + \Delta R_3^2 + \Delta R_4^2} + \Delta R_2$, to avoid an underestimation of the uncertainty.

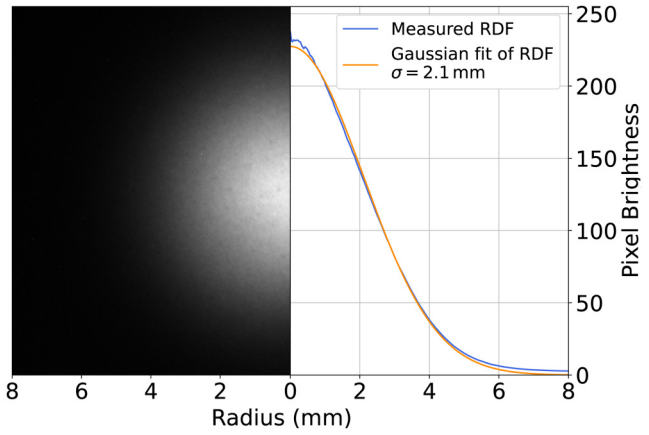

FIG. 7. The radial intensity function (RIF) on the right is calculated from an image of the detector camera shown on the left. A conversion factor is applied to convert the number of pixels to a distance.

TABLE II. Overview of all considered error sources and their related uncertainty.

Detector resolution:	$\Delta R_1 = 25\,\mu$m
Davisson–Calbick effect:	$\Delta R_2 = 41\,\mu$m
Uncertainty RIF:	ΔR_3
Uncertainty instrument function:	$\Delta R_4 = U_R$
Uncertainties distance:	Δd = 0.3 mm
	Δg = 0.1 mm
Uncertainty voltage:	ΔU = 0.1% of measured value

The MTE can be determined in two different ways. It can be calculated as a single shot measurement by directly inserting the measured radius in Eq. (3). Nevertheless, the single shot measurement is subject to a high degree of uncertainty. A more profound measurement can be done with a voltage scan. In this case, the radius at the detector is measured as a function of the applied voltage at the photocathode. The MTE is determined by fitting the data with Eq. (9). The MTE is the only fit parameter since voltage U, distances g and d, and the electron charge e are known,

$$R = (2g + d)\sqrt{\frac{\text{MTE}}{Ue}}. \tag{9}$$

The uncertainty of the radius is taken into account in the fit and is reflected in the uncertainty of the fit parameter. The uncertainties due to voltage ΔU and distances Δg and Δd are considered separately. The contribution of these values to the uncertainty of MTE is calculated for each single measurement of the voltage scan. The maximum value is added to the uncertainty of the fit parameter by Pythagorean addition to give the total uncertainty ΔMTE. All different error sources are summarized in Table II.

V. TRIPLE EVAPORATION Na–K–Sb PHOTOCATHODE

A. Growth procedure

After the commissioning of the new growth chamber, a Na–K–Sb photocathode was grown with the triple evaporation approach for the first time at October 15, 2024. This photocathode will be referred to as TWH013 in the following. A full molybdenum plug was inserted to the preparation system, degassed, and cleaned with argon sputtering. Before the growth, the deposition rate of all three sources was measured with the QCM to be 0.011 Å/s for Sb, 0.029 Å/s for Na, and 0.19 Å/s for K.

In Fig. 8, we show the growth procedure. The sample stage was heated to 100 °C, and the shutters of the Sb, K, and Na sources were simultaneously opened at $t = 0$ min. No increase in the photocurrent could be observed within the first 60 min. Therefore, the stage temperature was increased to 110 °C after 65 min, to enhance the chemical reaction of the materials. Shortly after, the photocurrent started to increase. The vacuum pressure during deposition was stable at 2×10^{-9} mbar. The laser power was reduced with an

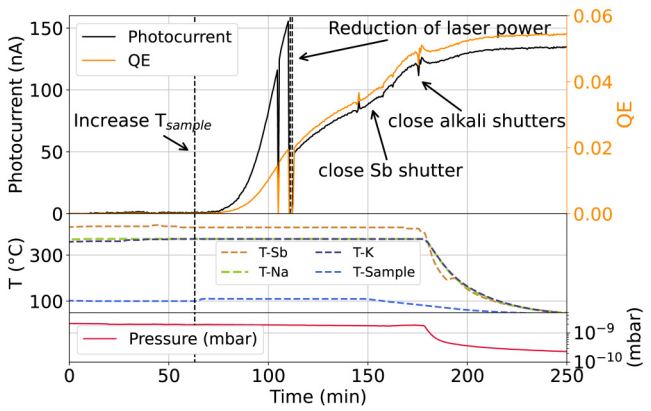

FIG. 8. Growth procedure of the photocathode TWH013. An increase of the photocurrent started shortly after the sample stage temperature was increased to 110 °C. Besides the photocurrent/QE, also the temperatures and the vacuum pressure are shown. The photocurrent was measured at 520 nm.

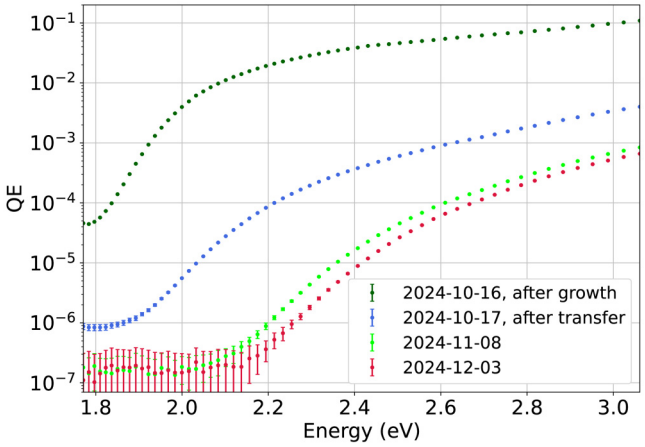

FIG. 9. Spectral response curve of the photocathode TWH013. The first curve was measured in the preparation system. The other curves were measured at PhoTEx.

additional ND 0.5 filter after 112 min to lower the extracted charge during the growth. The dips after 105 and 111 min are caused by temporarily switching off the power supply for the photocurrent measurement to check the darkcurrent and the photo response. At the end of the deposition, after 145 min, the shutters were opened and closed to maximize the photocurrent. Closing the alkali shutters reduced the photocurrent indicating an alkali deficiency, so they were opened again. The sample temperature was reduced, and the Sb source was closed 12 min later. After 175 min, the alkali shutters were closed, and the heaters of the sources were turned off. While cooling down, the QE further increased and stabilized at QE = 5.5% at 520 nm. The photocurrent was monitored over night showing a $1/e$ lifetime of 64 h.

In Fig. 9, we show the spectral response measurement of TWH013. One day after growth, QE = 3.7% was measured at 520 nm (2.38 eV). An XPS measurement of the photocathode was done, showing that the antimony was not fully reacted with respect to the Sb 3d core level. A detailed study on the XPS data will be published elsewhere. After the XPS measurement, the QE was decreased to 0.7%. The photocathode was then moved into the vacuum suitcase and transferred to PhoTEx.

B. Characterization at PhoTEx

The photocathode TWH013 was transferred to PhoTEx for the commissioning of the instrument. The spectral response of the photocathode was regularly measured and is shown in Fig. 9. The first curve was measured in the preparation chamber of the photocathode laboratory one day after the growth on October 16, 2024. An increased pressure occurred during the transfer with bursts up to high 10^{-9} mbar for 1.5 h when moving the transfer arm. This leads to a reduced quantum efficiency of just QE = 0.04 % at 2.38 eV. Note that the recipe was not yet optimized for a long lifetime. The growth recipe is currently being optimized, and the vacuum suitcase and load locks are being improved to optimize the vacuum conditions during the transfer.

After the transfer, the quantum efficiency further decreased with a $1/e$ lifetime of just few hours but stabilized at a QE in the 10^{-6} range due to the excellent vacuum conditions at PhoTEx. After 7 weeks, there was still a detectable photocurrent. Together with the decrease in QE, the effective workfunction appears to shift toward higher energies. Nevertheless, the high sensitivity of PhoTEx allows the measurement of the quantum efficiency down to $QE = 1 \times 10^{-6}$.

Along with the spectral response, the reflectance was measured for an angle of incidence of 38.7°. As the reflectance changes less than the QE, only a selection of the measurements is shown in Fig. 10. From the reflectance curves, the color of the photocathode

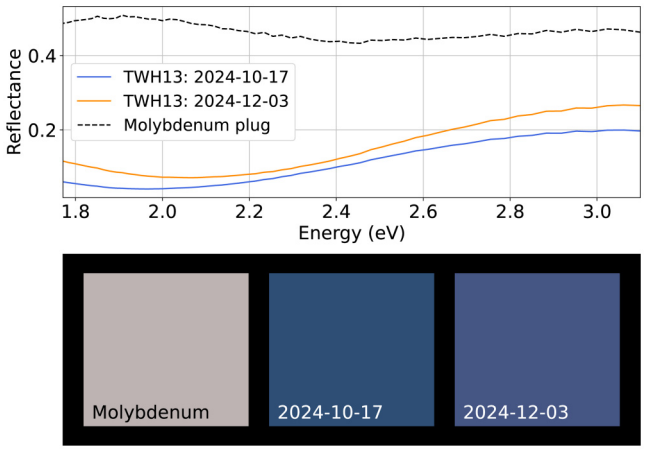

FIG. 10. Reflectance curves of the photocathode TWH013. From the reflectance, the color was determined using the CIE 1931 color space. The reflectance and color of the pure molybdenum plug were measured as a reference.

TABLE III. Colorimetry data of the photocathode TWH013 measured at 38.7° angle of incidence.

2024-10-17	XYZ = 0.071; 0.073; 0.180 sRGB = 45; 77; 117
2024-12-03	XYZ = 0.100; 0.097; 0.231 sRGB = 69; 86; 131
Molybdenum	XYZ = 0.452; 0.463; 0.492 sRGB = 188; 178; 179

was determined as described above. The photocathode becomes slightly brighter and more purple as it ages. The reflectance of the pure molybdenum at the edge of the plug was also measured as a reference. The XYZ and sRGB values are listed in Table III.

The MTE was measured 67 days after the growth of the photocathode, on December 22, 2024. A first voltage scan ranging from 600 to 6500 V with steps of 100 V was performed at 450 nm (2.76 eV). The voltage of the MCP was adjusted during the scan to ensure uniform brightness of the images with a fixed exposure time of 1 s. The Helmholtz coils were used to steer the beam to the center of the detector. The scan is shown in Fig. 11 and results in a measured value of MTE = (135.4 ± 1.6) meV. This corresponds to a relative uncertainty of 2%. Each of the 61 measured points was also analyzed as a single shot measurement using Eq. (3). All single shot measurements agree with the voltage scan within the limits of uncertainty. Nevertheless, the uncertainties of the single shot measurements are significantly larger, ranging from 6% up to 15% for small electron beam radii at the detector. An optical power of $P_\gamma = 28$ nW was used for this measurement. Together with the known QE, the average number of electrons in the system N_e can be determined with Eq. (10). The electron flight time τ is given by

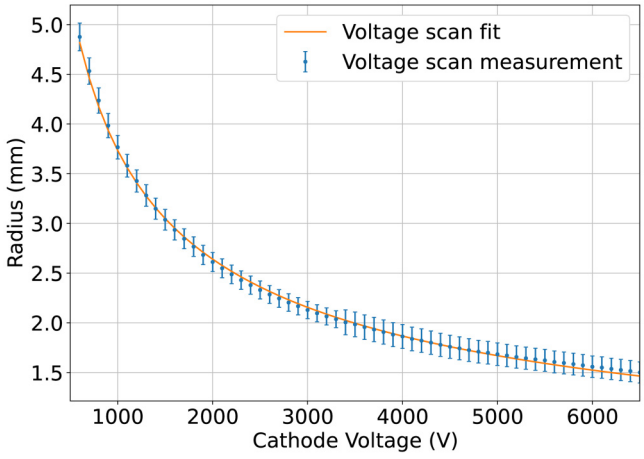

FIG. 11. Voltage scan of the photocathode TWH013 to measure the MTE at 450 nm. The electron beam radius at the detector is measured as a function of the bias voltage at the cathode and fitted with Eq. (9). From the fit parameter, the MTE can be determined to be MTE = (135.4 ± 1.6) meV.

the system parameters g, d, and U, the electron mass m_e, and charge e. The initial longitudinal velocity of the electron v_{z0} is small compared to the acceleration and can be neglected for rough approximation,

$$N_e = \frac{I}{e}\tau = \mathrm{QE}\frac{P_\gamma \lambda}{hc}\tau,$$
$$\tau = -\frac{g m_e v_{z0}}{Ue} + \sqrt{\left(\frac{g m_e v_{z0}}{Ue}\right)^2 + \frac{2g^2 m_e}{Ue}} + \frac{d}{\sqrt{v_{z0}^2 + \frac{2Ue}{m_e}}}. \quad (10)$$

In the best case, the number of electrons in the system at the same time N_e should be close to 1 to avoid electron–electron interaction. With a current of $I = 2 \times 10^{-11}$ A and $N_e = 1.5$, we do not expect any space charge effects. In the case of a photocathode with higher QE, the optical power should be attenuated using ND filters.

Additionally, the MTE was measured as a function of the wavelength from 400 to 530 nm. For longer wavelengths, a full voltage scan is no longer possible due to the low remaining quantum efficiency of the photocathode. Therefore, PhoTEx is able to measure the MTE up to a QE of about 0.001%. For each wavelength, a voltage scan from 700 to 6500 V with a step width of 200 V was performed to determine the MTE. The data are plotted in Fig. 12 as a function of the photon energy. This presentation allows an easy determination of the effective workfunction by fitting the data with a linear function. The effective workfunction ϕ_{eff} is the barrier, and the electron has to overcome in order to get emitted.[11] In a first-order approximation, we expect MTE = 0 meV when the excitation energy is equal to ϕ_{eff} as stated in Eq. (2). From the linear fit, we obtain $\phi_{\mathrm{eff}} = 2.0$ eV.

Maxson *et al.* measured the MTE of a sequentially deposited Na–K–Sb photocathode on a stainless steel substrate to be 134 meV at a wavelength of 532 nm.[36] The results presented here are significantly smaller with (60 ± 2) meV at 530 nm. However, the TWH013 photocathode was measured at an aged state. As shown in Fig. 9, the aging leads to a shift in the work function toward

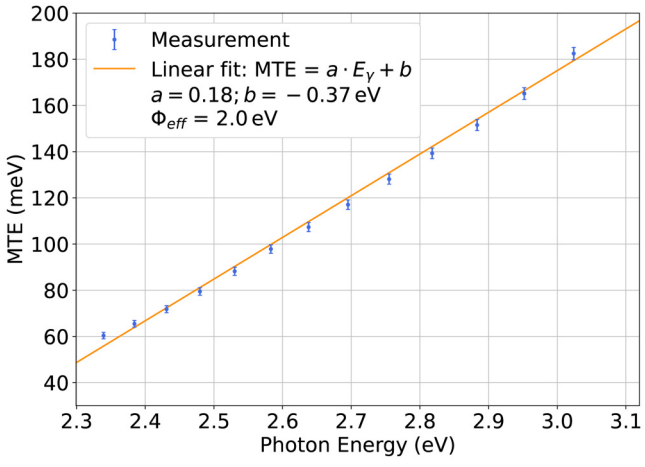

FIG. 12. Wavelength scan of photocathode TWH013. The data can be fitted with a linear function to determine the effective workfunction $\phi_{\mathrm{eff}} = 2.0$ eV.

higher energies and, therefore, reducing the MTE. In the range considered by the wavelength scan, the MTE is already tending toward the thermal limit. The slope of the linear function is, therefore, smaller then the expected value $a = 1/3$, which has already been observed in earlier studies, and the calculated effective workfunction is underestimated.[37] This has to be compared with other, less aged photocathodes in the future.

VI. CONCLUSION

A new preparation chamber was set up at the photocathode laboratory at HZB. The system was upgraded with effusion cells for the alkali metals and a thermal cracker cell for antimony. As a result, more photocathodes can be grown without changing the sources, which improves the base pressure of the vacuum system and the reproducibility of the photocathode recipes as well as the time required for the preparation and growth of the photocathodes. All three sources are now pointed at the same position, allowing photocathode growth using the triple evaporation method, where all three materials are deposited simultaneously.

The novel characterization system PhoTEx is able to measure the MTE, QE, reflectance, and lifetime of the photocathodes. PhoTEx is an instrument allowing the measurement of all physical key parameters in one compact setup without moving the sample. This is of major importance, as any transfer to another system may harm the photocathode. PhoTEx allows characterization of the photocathodes in the full visible regime. The spectral resolved measurement of the reflectance enables the study of a new parameter: the color of the photocathode. The color has already been subject of much discussion in the photocathode community, to allow an easy first assessment of the photocathode quality. For the first time, the photocathode colorimetry allows a systematic analysis of this parameter. The high resolution of PhoTEx allows the characterization over a long period of time. The QE can be measured down to $QE = 1 \times 10^{-6}$ and the MTE up to an efficiency of at least $QE = 1 \times 10^{-5}$. The MTE can be measured by a single shot measurement or a voltage scan. Since the voltage scan consists of several measurements, the uncertainty is significantly smaller with this method.

After commissioning, a triple evaporation photocathode was grown with the new preparation system. To the best of our knowledge, we give the first detailed description of the Na–K–Sb triple evaporation growth procedure. Directly after growth, the photocathode reached a QE of 5.5% at 520 nm. The photocathode was transferred to PhoTEx and analyzed for more then 2 months. The degradation of the quantum efficiency, reflectance, and colorimetry was studied at PhoTEx. The MTE was measured with two different methods, and both results agree with each other within the limits of uncertainty. Overall, all measurements are self-consistent and provide a credible dataset.

In the future, PhoTEx will be used to routinely study the photocathodes grown at HZB regarding their QE, MTE, and lifetime. This will help to further improve the photocathode recipes at the new triple evaporation growth system. Together they form the basis of new photocathodes with high QE and low MTE, which are crucial for the generation of high-brightness electron beams at existing and future accelerator facilities.

ACKNOWLEDGMENTS

The authors gratefully acknowledge the support from Axel Neumann and Jens Völker from Helmholtz-Zentrum Berlin as well as the consultancy and scientific exchange with Laura Monaco and Daniele Sertore from INFN Milano - LASA and Lee Jones from STFC Daresbury Laboratory. Work supported by German Bundesministerium für Bildung und Forschung, Land Berlin, grants of Helmholtz As- sociation, and Deutsche Forschungsgemeinschaft (DFG): No. CO 1509/10-1 — MI 2917/1-1.

AUTHOR DECLARATIONS

Conflict of Interest

The authors have no conflicts to disclose.

Author Contributions

J. Dube: PhoTEx—conceptualization (lead); Investigation (lead); Data curation (lead); Formal analysis (lead); Writing – original draft (lead); Visualization (lead); Writing – review & editing (equal). **J. Kühn:** Conceptualization (lead); Investigation (equal); Project administration (equal); Supervision (equal); Writing – original draft (equal); Writing – review & editing (equal). **C. Wang:** Investigation (equal); Data curation (equal); Writing – review & editing (equal). **S. Mistry:** Funding acquisition (equal); Investigation (supporting); Writing – review & editing (equal). **G. Klemz:** Investigation (supporting); Writing – review & editing (equal). **A. Galdi:** Investigation (equal); Writing – review & editing (equal). **T. Kamps:** Supervision (equal); Funding acquisition (lead); Project administration (equal); Writing – review & editing (equal).

DATA AVAILABILITY

The data that support the findings of this study are available from the corresponding author upon reasonable request.

REFERENCES

[1]Z. T. Zhao, Z. Wang, C. Feng, S. Chen, and L. Cao, "Energy recovery linac based fully coherent light source," Sci. Rep. **11**, 23875 (2021).
[2]A. Neumann, B. Alberdi, T. Birke, P. Echevarria, D. Eichel, F. Falkenstern, R. Fleischhauer, A. Frahm, F. Goebel, A. Heugel *et al.*, "bERLinPro becomes SEALab: Status and perspective of the energy recovery linac at HZB," in *Proceedings of the 13th International Particle Accelerator Conference, IPAC'22* (JACoW Publishing, Geneva, Switzerland, 2022), pp. 1110–1113.
[3]P. Emma, R. Akre, J. Arthur, R. Bionta, C. Bostedt, J. Bozek, A. Brachmann, P. Bucksbaum, R. Coffee, F.-J. Decker *et al.*, "First lasing and operation of an ångstrom-wavelength free-electron laser," Nat. Photonics **4**, 641–647 (2010).
[4]J. Schaber, R. Xiang, and N. Gaponik, "Review of photocathodes for electron beam sources in particle accelerators," J. Mater. Chem. C **11**, 3162–3179 (2023).
[5]D. Filippetto, P. Musumeci, R. Li, B. Siwick, M. Otto, M. Centurion, and J. Nunes, "Ultrafast electron diffraction: Visualizing dynamic states of matter," Rev. Mod. Phys. **94**, 045004 (2022).
[6]A. H. Zewail, "4D ultrafast electron diffraction, crystallography, and microscopy," Annu. Rev. Phys. Chem. **57**, 65–103 (2006).
[7]B. Alberdi Esuain, J.-G. Hwang, A. Neumann, and T. Kamps, "Novel approach to push the limit of temporal resolution in ultrafast electron diffraction accelerators," Sci. Rep. **12**, 13365 (2022).

[8]T. Rao and D. H. Dowell, "An engineering guide to photoinjectors," arXiv.1403.7539 (2014).
[9]H. Lee, S. Karkare, L. Cultrera, A. Kim, and I. V. Bazarov, "Review and demonstration of ultra-low-emittance photocathode measurements," Rev. Sci. Instrum. **86**, 073309 (2015).
[10]P. Schmüser, M. Dohlus, J. Rossbach, C. Behrens, C. Behrens, M. Dohlus, and J. Rossbach, *Free-Electron Lasers in the Ultraviolet and X-Ray Regime: Physical Principles, Experimental Results, Technical Realization*, Springer Tracts in Modern Physics Vol. 258, 2nd ed. (Springer Nature, 2014).
[11]P. Saha, O. Chubenko, J. Kevin Nangoi, T. Arias, E. Montgomery, S. Poddar, H. A. Padmore, and S. Karkare, "Theory of photoemission from cathodes with disordered surfaces," J. Appl. Phys. **133**, 053102 (2023).
[12]D. H. Dowell, I. Bazarov, B. Dunham, K. Harkay, C. Hernandez-Garcia, R. Legg, H. Padmore, T. Rao, J. Smedley, and W. Wan, "Cathode R&D for future light sources," Nucl. Instrum. Methods Phys. Res. Sect. A **622**, 685–697 (2010).
[13]G. Wang, R. Pandey, N. A. Moody, and E. R. Batista, "Degradation of alkali-based photocathodes from exposure to residual gases: A first-principles study," J. Phys. Chem. C **121**, 8399–8408 (2017).
[14]E. Wang, V. N. Litvinenko, I. Pinayev, M. Gaowei, J. Skaritka, S. Belomestnykh, I. Ben-Zvi, J. C. Brutus, Y. Jing, J. Biswas, J. Ma, G. Narayan, I. Petrushina, O. Rahman, T. Xin, T. Rao, F. Severino, K. Shih, K. Smith, G. Wang, and Y. Wu, "Long lifetime of bialkali photocathodes operating in high gradient superconducting radio frequency gun," Sci. Rep. **11**, 4477 (2021).
[15]M. A. Schmeißer, S. Mistry, H. Kirschner, S. Schubert, A. Jankowiak, T. Kamps, and J. Kühn, "Towards the operation of Cs-K-Sb photocathodes in superconducting rf photoinjectors," Phys. Rev. Accel. Beams **21**, 113401 (2018).
[16]C. Cocchi, S. Mistry, M. Schmeißer, R. Amador, J. Kühn, and T. Kamps, "Electronic structure and core electron fingerprints of caesium-based multi-alkali antimonides for ultra-bright electron sources," Sci. Rep. **9**, 18276 (2019).
[17]S. Mistry, T. Kamps, J. Kühn, and C. Wang, "Multi-alkali antimonide photocathode development for high brightness beams," in *Proceedings of the 13th International Particle Accelerator Conference, IPAC'22* (JACoW Publishing, Geneva, Switzerland, 2022), pp. 2610–2613.
[18]S. Mistry, J. Dube, T. Kamps, J. Kuehn, and C. Wang, "Evaluation of the in-situ photocathode handling for SRF photoinjector of SEALab," in *Proceedings of the 13th International Particle Accelerator Conference, IPAC'22* (JACoW Publishing, Geneva, Switzerland, 2023), pp. 4240–4242, issue: 14.
[19]S. Rozhkov, V. Bakin, V. Rusetsky, D. Kustov, V. Golyashov, A. Demin, H. Scheibler, V. Alperovich, and O. Tereshchenko, "Na_2 KSb/Cs_x Sb interface engineering for high-efficiency photocathodes," Phys. Rev. Appl. **22**, 024008 (2024).
[20]J. Feng, J. Nasiatka, W. Wan, T. Vecchione, and H. A. Padmore, "A novel system for measurement of the transverse electron momentum distribution from photocathodes," Rev. Sci. Instrum. **86**, 015103 (2015).
[21]L. Jones, D. Juarez-Lopez, H. Scheibler, A. Terekhov, B. Militsyn, C. Welsch, and T. Noakes, "The measurement of photocathode transverse energy distribution curves (TEDCs) using the transverse energy spread spectrometer (TESS) experimental system," Rev. Sci. Instrum. **93**, 113314 (2022).
[22]D. Sertore, M. Bertucci, A. Bosotti, D. Giove, L. Monaco, and R. Paparella, "Assembly and characterization of low-energy electron transverse momentum measurement device (TRAMM) at INFN LASA," in *Proceedings of the 13th International Particle Accelerator Conference, IPAC'22* (JACoW Publishing, Geneva, Switzerland, 2022).
[23]M. Abo-Bakr, N. Al-Saokal, W. Anders, Y. Bergmann, K. Bürkmann-Gehrlein *et al.*, "The berlin energy recovery linac project BERLinPro—Status, plans and future opportunities," in *Proceedings of the 63rd ICFA Advanced Beam Dynamics Workshop, ERL'19* (JACoW Publishing, Geneva, Switzerland, 2020).
[24]T. Kamps, M. Abo-Bakr, B. Alberdi, T. Birke, P. Echevarria, E. Ergenlik, R. Fleischhauer, A. Frahm, H. Huck, G. Klemz *et al.*, "Accelerator physics experiments at the versatile SRF photoinjector of SEALab," in *Proceedings of the 14th International Particle Accelerator Conference, IPAC'23* (JACoW Publishing, Geneva, Switzerland, 2023), pp. 2115–2118.
[25]J. Kühn, N. Al-Saokal, M. Bürger, M. Dirsat, A. Frahm, A. Jankowiak, T. Kamps, G. Klemz, S. Mistry, A. Neumann, and H. Plötz, "Thermal load studies on the photocathode insert with exchangeable plug for the bERLinPro SRF-photoinjector," in *Proceedings of the 19th International Conference on RF Superconductivity, SRF'19* (JACoW Publishing, Geneva, Switzerland, 2019).
[26]J. Kühn, J. Borninkhof, M. Bürger, A. Frahm, A. Jankowiak, T. Kamps, M. Schmeißer, M. Schuster, P. Murcek, J. Teichert, and R. Xiang, "UHV photocathode plug transfer chain for the bERLinPro SRF-photoinjector," in *Proceedings of the 8th International Particle Accelerator Conference, IPAC'2017* (JACoW Publishing, Geneva, Switzerland, 2017).
[27]W. E. Spicer, "Photoemissive, photoconductive, and optical absorption studies of alkali-antimony compounds," Phys. Rev. **112**, 114 (1958).
[28]D. Dowell and J. F. Schmerge, "Quantum efficiency and thermal emittance of metal photocathodes," Phys. Rev. Special Topics—Acceler. Beams **12**, 074201 (2009).
[29]CST Studio Suite version 2024.05, Dassault Systemes Deutschland GmbH, Vélizy-Villacoublay, France (2024), https://www.3ds.com/products/simulia/cst-studio-suite
[30]K. Flottmann, S. Lidia, and P. Piot, "Recent improvements to the ASTRA particle tracking code," Technical Report (Lawrence Berkeley National Lab.(LBNL), Berkeley, CA (United States), 2003).
[31]J. Kruschwitz, *Field Guide to Colorimetry and Fundamental Color Modeling*, edited by J. Greivenkamp (SPIE Press, 2018), Vol. FG42.
[32]CIE 2022, "CIE standard illuminant D65," International Commission on Illumination (CIE), Vienna, Austria (2022).
[33]CIE 2018, "CIE 1931 colour-matching functions, 2 degree observer (data table)," International Commission on Illumination (CIE), Vienna, Austria (2018). .
[34]C. J. Davisson and C. J. Calbick, "Electron lenses," Phys. Rev. **42**, 580 (1932).
[35]L. Yu, W. Wan, W.-X. Tang, and J. Feng, "Systematic analysis of a compact setup to measure the photoemitted electron beam transverse momentum and emittance," Rev. Sci. Instrum. **92**, 013302 (2021).
[36]J. Maxson, L. Cultrera, C. Gulliford, and I. Bazarov, "Measurement of the tradeoff between intrinsic emittance and quantum efficiency from a NaKSb photocathode near threshold," Appl. Phys. Lett. **106**, 234102 (2015).
[37]A. Kachwala, P. Saha, P. Bhattacharyya, E. Montgomery, O. Chubenko, and S. Karkare, "Demonstration of thermal limit mean transverse energy from cesium antimonide photocathodes," Appl. Phys. Lett. **123**, 044106 (2023).